英文レター誌「SOLA」論文の一段組印刷への移行のお知らせ

竹見哲也

京都大学防災研究所/SOLA 編集委員長

英文レター誌 SOLA は，2005 年の創刊以来（田中，2005），既に第 18 巻を数えています．最近では，気象集誌との連携を深め，時宜を得たテーマで気象集誌との合同特別号も発刊しています．編集委員会には国内外から第一線の研究者に参画していただいており，国外からの投稿論文数も堅調に推移しています．被引用件数も年々伸びており，特にインパクトファクターも直近数年で上昇傾向にあり，国際的な認知度も着実に向上しています．

SOLA では，これまで多くの他誌と同様に印刷して論文を読むことを想定し，二段組のスタイルで組版し PDF を作成してきました．一方近年では，論文をパソコンやタブレットなど電子媒体で読むスタイルも一般的になっています．電子媒体の画面上では，一段組のほうが読みやすい面がありますが，今後も印刷して読まれることも少なくないと思われます． SOLA 編集委員会では，これらの両面に対応した，一段組での組版について検討を進め，2023 年より一段組での PDF 作成に変更することといたしましたので，お知らせいたします．

一段組のサンプルを添付します．これは，Komatsu and Nishimura (2022)を一段組にしたものです．今後投稿される際には，一段組を想定して図表をご作成いただければと思います．

参考文献

田中博，2005：英文レター誌「SOLA」の創刊のお知らせ．天気，**52**, 40

Komatsu, A., and K. Nishimura, 2022: Calculation of snowdrift distribution over complex topography to improve the accuracy of snow avalanche warning systems. SOLA, **18**, 71−78.

Calculation of Snowdrift Distribution over Complex Topography to Improve the Accuracy of Snow Avalanche Warning Systems

Asami Komatsu[1, 2] and Kouichi Nishimura[1, 2]

[1]*Japan Weather Association*, *Sapporo*, *Japan*
[2]*Nagoya University*, *Nagoya*, *Japan*

(Manuscript received 11 November 2021, accepted 16 February 2022)

Abstract We introduce a new procedure to evaluate the snowdrift distribution over complex topography and improve the accuracy of snow avalanche warning systems. We select the Niseko region, Japan, as the target area, and first obtain the wind distribution map at a 50-m grid spacing for 16 wind directions. We then employ these maps to calculate the amount of snow erosion and deposition. We present a case study to demonstrate that the model output agrees fairly well with measurements of local wind speed and observed snowdrift distribution. While improvements can be made to improve the accuracy of the model results, including more comprehensive calculation procedures and quantitative comparisons of snowdrift formation and evolution, it appears that the presented snowdrift analysis is an effective tool that can be incorporated into a snow avalanche warning system that employs a simple snow-cover model.

Citation: Komatsu, A., and K. Nishimura, 2022: Calculation of snowdrift distribution over complex topography to improve the accuracy of snow avalanche warning systems. *SOLA*, **18**, 71−78, doi:10.2151/sola.2022-012.

1. Introduction

Snow avalanches cause substantial damage to not only the traffic facilities but in the various aspects of human activities in the snowy region. Komatsu and Nishimura (2020) developed a simple snow-cover model (SSCM), which only requires surface air temperature and precipitation as input data, to evaluate snow avalanche hazards. The SSCM can reproduce, within reasonable accuracy, changes in snowpack properties and snow avalanche incidents. However, it was revealed that the effect of wind over complex topography should be additionally considered. Wind speed is generally high near an avalanche source area, such that greater snow transport and accumulation occur on the leeward slope. Snow drifting should therefore be incorporated into the SSCM to improve the accuracy.

Lehning et al. (2008) developed the Alpine3D model, which incorporates wind fields calculated using the ARPS (Advanced Regional Prediction System) meso-scale atmospheric model (Xue et al. 1995), to evaluate the snow distribution across steep alpine terrain. Vionnet et al. (2017) also simulated snow accumulation in alpine terrain using the Meso-NH/Crocus model. The former is a non-hydrostatic atmospheric model (Lafore et al. 1998), and the latter is a snowpack model (Brun et al. 1989). However, Japanese avalanche warning systems rarely consider heterogeneous snow distributions.

Here we developed a system to calculate snow transport and deposition across complex topography and coupled it to the SSCM. We then applied the procedure to the Niseko area in Hokkaido, Japan (Fig. 1). Although the altitude of Mt. Annupuri located in the study area is only about 1,300 m high, the snow is completely dry in winter and very popular among skiers. Therefore, the local communities and ski area managers strongly desire a more precise avalanche warning system. Furthermore, the Niseko town and National Research Institute for Earth Science and

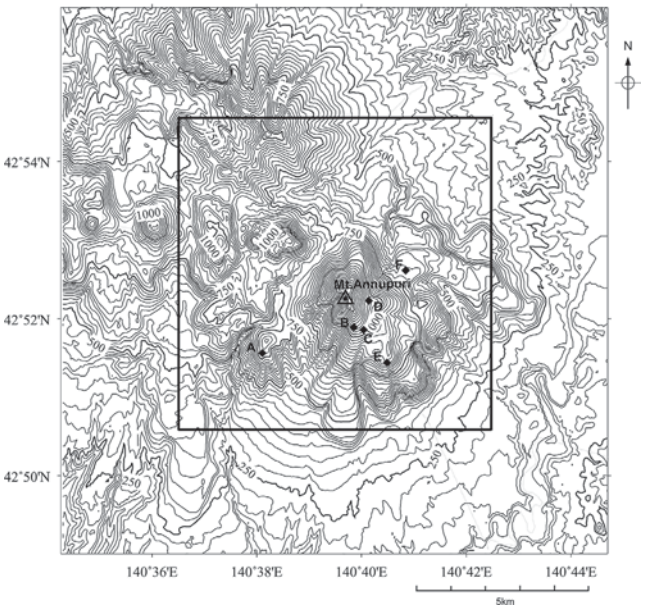

Fig. 1. Topographic map of the model domain across the Niseko region. Contours indicate the surface elevation (m). Detailed analyses are conducted within the area that is enclosed by the black square. The locations of the wind observation stations are also shown: Moiwa (A), Annupuri (B), Yunosawa (C), Hirafu (D), Village (E), and Hanazono (F).

Corresponding author: Asami Komatsu, Japan Weather Association, Kita 4-jo Nishi 23-chome, Chuo-ku, Sapporo-shi, Hokkaido 064-8555, Japan. E-mail: komatsu@jwa.or.jp.

Disaster Resilience (NIED) have established six propeller anemometers in the area (Fig. 1), which are useful to validate the model performance. Five of them are set at 3 m high and one at Hanazono is 10 m, and all the data are recorded every 10 minutes. We also attempted to simplify the procedures as much as possible to reduce the computational requirements and generate numerous simulations within a short period, which is ideal for modeling a snow avalanche scenario within one hour even using a low-spec computer.

2. Methodology

2.1 Model

Wind-induced snow transport can be divided into two general transport modes: saltation and suspension (Bagnold 1941). Here we apply continuum mixture theory to this turbulent mixture of air and snow. The particle concentrations in the suspension layer are calculated using the conservation equation for the snow–air mixture, and the wind field is calculated using the Reynolds-averaged Navier–Stokes equation. The saltation layer is included as the lower boundary condition. Our model consists of air flow and blowing snow simulations based on Uematsu et al. (1991) and Sato and Yasuda (2014). We first simulate the wind field over the terrain to obtain the friction velocity distributions and calculate the snowdrift transport. We then obtain erosion and/or deposition rates via the divergence of the snow transport rate. Generalized curvilinear coordinates along the surface topography are used during the calculations (Murakami et al. 1989).

a. Air flow simulation

Air flow was simulated based on the conservation of mass and momentum as follows:

$$\frac{\partial u_i}{\partial x_i} = 0 \tag{1}$$

and

$$\frac{\partial u_i}{\partial t} + \frac{\partial u_i u_j}{\partial x_j} = -\frac{1}{\rho}\frac{\partial p}{\partial x_i} + \frac{\partial}{\partial x_j}\left\{\upsilon_t\left[\frac{\partial u_i}{\partial x_j} + \frac{\partial u_j}{\partial x_i}\right]\right\}, \tag{2}$$

where x_i is the spatial coordinate system (x, y, z), u_i is the average wind speed vector (u, v, w; m s^{-1}), t is time (s), p is air pressure (kg m^{-1} s^{-2}), ρ is air density (1.29 kg m^{-3}), and υ_t (m^2 s^{-1}) is the coefficient of eddy viscosity. The standard k–ε model under the neutral condition was applied for υ_t as follows:

$$\upsilon_t = C_\mu \frac{k^2}{\varepsilon}, \tag{3}$$

$$\frac{\partial k}{\partial t} + \frac{\partial k u_j}{\partial x_j} = \frac{\partial}{\partial x_j}\left[\frac{\upsilon_t}{\sigma_k}\frac{\partial k}{\partial x_j}\right] + \upsilon_t\left[\frac{\partial u_i}{\partial x_j} + \frac{\partial u_j}{\partial x_i}\right]\frac{\partial u_i}{\partial x_j} - \varepsilon, \tag{4}$$

$$\frac{\partial \varepsilon}{\partial t} + \frac{\partial \varepsilon u_j}{\partial x_j} = \frac{\partial}{\partial x_j}\left[\frac{\upsilon_t}{\sigma_\varepsilon}\frac{\partial \varepsilon}{\partial x_j}\right] + C_{1\varepsilon}\frac{\varepsilon}{k}\upsilon_t\left[\frac{\partial u_i}{\partial x_j} + \frac{\partial u_j}{\partial x_i}\right]\frac{\partial u_i}{\partial x_j} - C_{2\varepsilon}\frac{\varepsilon^2}{k}, \tag{5}$$

where k is turbulent energy (m^2 s^{-2}), ε is the dissipation rate of turbulent energy (m^2 s^{-3}), and C_μ, $C_{1\varepsilon}$, $C_{2\varepsilon}$, σ_k, and σ_ε are constants. Here we used $C_\mu = 0.09$, $C_{1\varepsilon} = 1.44$, $C_{2\varepsilon} = 1.92$, $\sigma_k = 1.0$, and $\sigma_\varepsilon = 1.3$ from Launder and Spalding (1974).

At the inlet boundary condition, logarithmic vertical wind profiles were assumed in the model and the boundary conditions were set as

$$u = v = w = 0 \tag{6}$$

at the bottom and

$$u = u_{ini},\ v = v_{ini},\ w = 0 \tag{7}$$

at the top of the domain. Furthermore, the radiation condition of Orlanski (1976) is adopted at the lateral boundaries.

The friction velocity at the snow surface was obtained as

$$u_* = \frac{u(z)\kappa}{\ln(z/z_0)}, \tag{8}$$

where $u(z)$ is wind speed (m s^{-1}) at level z (m), κ is the von Karman constant (0.4), and z_0 is surface roughness (10^{-4} m, Kikuchi 1981). z_0 was used to define the logarithmic profile of wind velocity at the inflow boundary. Setting the inlet wind speed profile as logarithmic, the vertical profiles of k and ε were obtained as the function of the friction speed.

b. Snow transport simulation

The vertically integrated snowdrift flux q (kg m^{-1} s^{-1}) in the saltation layer is expressed as

$$q = \int_0^h (u_s \Phi) dz, \tag{9}$$

where u_s is the mean horizontal particle velocity (m s^{-1}), Φ is the snowdrift density (kg m^{-3}), and h is the thickness of the saltation layer (m). We employ the expression for q as proposed by Iversen et al. (1980):

$$q = C\left(\frac{\rho}{g}\right)\frac{|w_f|}{u_{*_t}} u_*^{\,2}(u_* - u_{*_t}), \tag{10}$$

where g is gravitational acceleration, w_f is the snow-particle fall speed, u_{*_t} is the threshold friction velocity, and C is a constant. Following Uematsu et al. (1991), w_f, C, and u_{*t} were set to 0.5 m s^{-1}, 1.0 and 0.2 m s^{-1} respectively for the simulations in this study.

The suspension is calculated using the following diffusion equation:

$$\frac{\partial \Phi}{\partial t} + \frac{\partial (\Phi u_i)}{\partial x_i} = \frac{\partial}{\partial x_i}\left(\upsilon_s \frac{\partial \Phi}{\partial x_i}\right) - \frac{\partial (w_f \Phi)}{\partial x_3}, \tag{11}$$

where Φ is snowdrift density (kg m^{-3}) in the suspension layer and υ_s is the eddy diffusion coefficient of snow assumed to be equal the momentum diffusivity of υ_t.

The snowdrift density at the upper boundary is expressed as

$$\Phi_H = \frac{P_{re}}{|W_f|}, \tag{12}$$

where P_{re} is the snowfall rate (kg m^{-2} s^{-1}). The upper boundary of suspension is the height where snowdrift density becomes zero.

The lower boundary of the suspension layer is in contact with the saltation layer. Therefore, the mean snowdrift density of the saltation layer Φ_h, which can be obtained by dividing q with u_s (= u_h) and h, is considered the lower boundary condition of the suspension layer. We note that h may change with the development of wind-driven snow transport; however, in this study, we assumed a constant thickness of 0.25 m which is the height of the first layer above the ground.

c. Deposition and erosion rates

The snowdrift rate S (kg m^{-2} s^{-1}) is defined as the mass of snow that accumulates on a unit horizontal area per unit time, and is calculated as the sum of the deposition rate D and erosion rate E:

$$S = D - E. \tag{13}$$

D and E are expressed as follows:

$$D = |w_f| \Phi_h \tag{14}$$

and

$$E = \frac{q|w_f|}{u_h h}. \tag{15}$$

The snow depth change within a unit time H (m) is then obtained by dividing S by the new snow density (10^2 kg m^{-3}).

d. Set-up of the numerical simulation

A numerical simulation method of SIMPLER developed by Patankar (1981) is applied to obtain a three-dimensional wind field; both the advection and the diffusion terms are combined and discretized with the exponential scheme. The wind field over the Niseko region is calculated using a digital elevation map with a 50-m grid interval that was supplied by the Geospatial Information Authority of Japan. The modeled atmospheric field spans 14 × 14 × 3.5 km in the $X \times Y \times Z$ domain. A stretched grid of 25 layers, in which 11 layers exist in the lowest 10 m, was applied for the vertical one. We hereafter focused on the 10 × 10 km area indicated by the black square in Fig. 1, which covers all the ski fields and wind measurement locations.

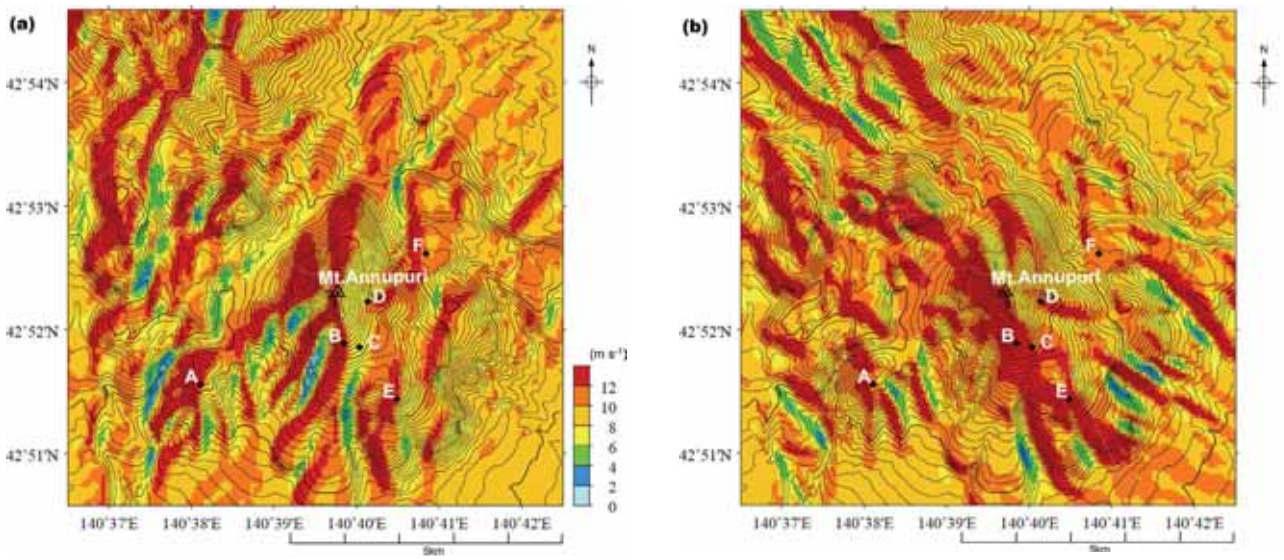

Fig. 2. Calculated wind speed distributions (shade) for the period when winds of 10 m s^{-1} at 10 m above the surface blew into the domain from the corresponding boundary, for winds from the (a) WNW and (b) SW. Contours indicate the surface elevation (m).

Table 1. Statistical analysis of simulated and observed wind speeds at sites across the Niseko region in February 2020. The number of samples (*n*), correlation coefficient (*R*), mean bias (observed value – model value), and root mean square error (RMSE) are provided.

	Moiwa	Annupri	Yunosawa	Hirafu	Village	Hanazono
n	654	221	696	696	696	659
R	0.84	0.87	0.81	0.76	0.81	0.82
Bias (m s^{-1})	1.5	0.5	0.9	1.2	−0.5	0.7
RMSE (m s^{-1})	3.3	3.1	2.5	2.8	2.8	2.5

3. Numerical simulation results

3.1 Wind distribution

We first calculated the wind speed distributions when winds of 10 m s^{-1} at 10 m high blew into the domain from the corresponding boundary and binned each wind calculation into the appropriate 16 wind directions; all of the data were then stored as look-up tables. Figure 2 shows the cases for the WNW and SW, where higher wind speeds are observed across the windward area of the high-altitude region, and lower wind speeds on the leeward side of the mountain and in the valley. We then set the Kucchan AMeDAS (KA) automatic weather station, which is operated by the Japan Meteorological Agency (JMA) and located 8.5 km ENE of the summit of Mt. Annupuri, as the reference point in this study. Although KA is outside of the calculation domain in Fig. 1, we confirmed that the wind speeds and directions at KA are approximately the same as those at the easternmost grid point at the same latitude in Fig. 1 and set that point as the virtual KA reference point; we note that these two points are separated by flatlands. Furthermore, the wind directions and speeds at the reference point are almost the same as the boundary conditions for all of the 16 wind directions, with the differences being less than 0.5 m s^{-1}. We subsequently obtained the ratios between the wind speed data at KA and all of the data in the domain for the 16 wind directions. We can reasonably calculate the wind speed distribution in the domain by multiplying the wind speed at KA by the ratio map obtained for each wind direction if we assume that the ratio does not vary significantly for different wind speeds. We confirmed that the wind directions and speeds at the reference point were almost the same as the boundary conditions for all cases. The time series of hourly wind speed at the six observation points was calculated for one month (February 2020). Three agreement scores [i.e., mean bias, RMSE and correlation coefficient between the observed and simulated wind speeds at the six sites] are listed in Table 1, and the time series at Moiwa and Village are shown in Fig. 3. The model worked reasonably well, as the correlation coefficients for all of the sites are ~0.8, the biases are within ± 1.5 m s^{-1}, and the RMSEs are 2.5−3.3 m s^{-1}. We also note that the periods of strong wind during 17−18 and 22−24 February are reproduced by the model fairly well. Although the considerable differences are occasionally found, it is probably caused by the grid size of DEM; 50-m may be not fine enough.

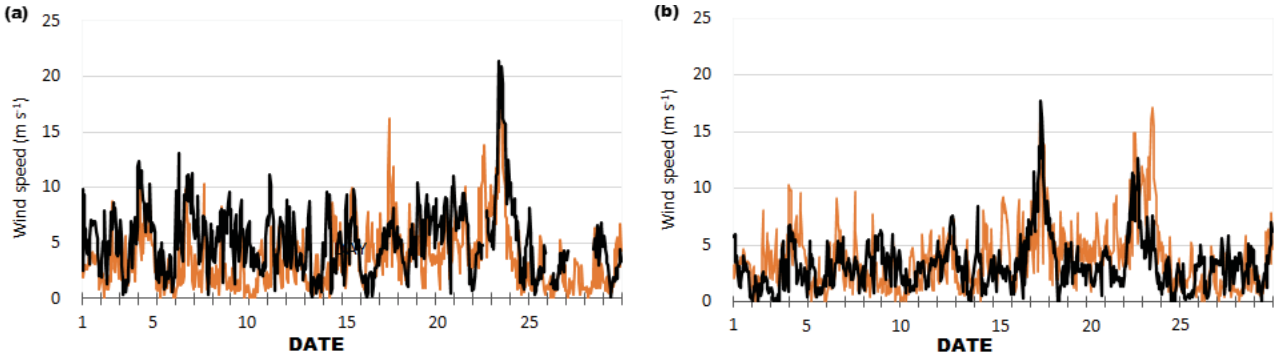

Fig. 3. Time series of observed and calculated wind speeds in February 2020. (a) Moiwa station (A in Fig. 1). (b) Village station (E in Fig. 1). The observed and calculated wind speeds are shown as black and colored lines, respectively.

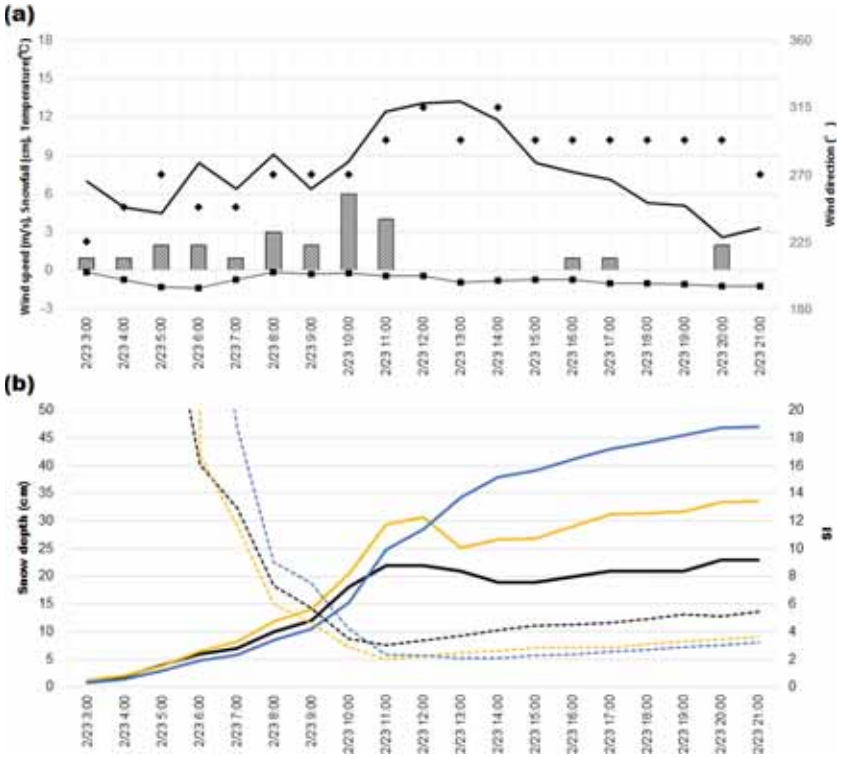

Fig. 4. (a) Time series of observed meteorological variables at KA during the case study on 23 February 2020. The wind speed (solid line), wind direction (diamonds), snowfall (gray boxes), and temperature (line with solid squares) are shown. (b) Solid lines show the snow depth at KA (observed, black), G (calculated, yellow), and H (calculated, blue). Dotted lines indicate the SI values calculated with the SSCM at KA (black), G (yellow), and H (blue). The sites G (Osawa) and H (Harunotaki) are the locations where snow avalanche accidents have previously been reported.

3.2 Snowdrift formation

We obtained numerical results for snowdrift formation across the target area. Here we introduce the results for 23 February 2020 as a case study, when an extra-tropical cyclone passed over Hokkaido and brought strong winds and snowfall. Figure 4a shows the meteorological conditions recorded at KA. High wind speeds were observed between 11:00 and 14:00 local time (LT), and the snow depth increased by nearly 25 cm.

Since the wind directions and speeds at the reference point of KA, are almost the same as the boundary conditions for all of the wind directions, we first divided the observed hourly wind speed at KA into three categories: less than 5, 5 to 10, and above 10 m s^{-1}. We then obtained the snow deposition and erosion rates over the target area for 5, 10, and 15 m s^{-1} based on the KA wind direction and the wind speed ratio distribution across the study area. We set the less than 5, 5 to 10, and above 10 m s^{-1} wind speeds at KA to 5, 10, and 15 m s^{-1}, respectively, and evaluated the change in snow depth in each grid cell by multiplying the deposition and erosion rates by their associated durations. Snowfall rates of 0−6 cm h^{-1}, assumed to be uniform over the area, are also included in the calculations (Fig. 4a).

Example of temporal changes in the snow depth distributions is shown in Fig. 5. The snow depth is evenly distribut-

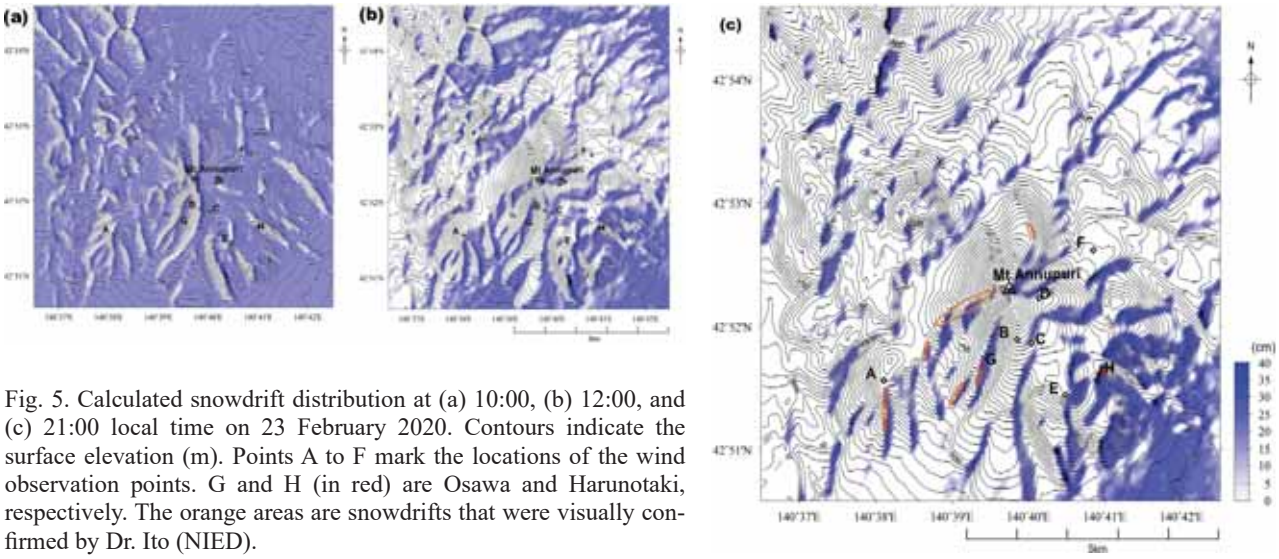

Fig. 5. Calculated snowdrift distribution at (a) 10:00, (b) 12:00, and (c) 21:00 local time on 23 February 2020. Contours indicate the surface elevation (m). Points A to F mark the locations of the wind observation points. G and H (in red) are Osawa and Harunotaki, respectively. The orange areas are snowdrifts that were visually confirmed by Dr. Ito (NIED).

ed across the entire area at 10:00 LT (Fig. 5a). However, the snow distribution was becoming localized by 12:00 LT (Fig. 5b) as the wind speed increased. An uneven snow distribution was clearly recognized by 21:00 LT (Fig. 5c), whereby snow was removed from the windward side of the ridge and accumulated on the leeward side and valley. We overlaid the snowdrift observations of Dr. Y. Ito acquired in March 2021 (pers. comm.) in Fig. 5c. We cannot make a direct comparison of the calculated drift distribution and observations because the former is based on a single storm event, whereas the latter represents the observed accumulation for almost an entire winter. However, we note that the locations of the snowdrifts in the region agree fairly well.

Finally, we applied the above case to assess its effectiveness in avalanche warning. Two locations (G and H in Fig. 5c) were selected for the analysis. In both G (Osawa) and H (Harunotaki), where substantial snow accumulates, numerous snow avalanche accidents have previously been reported (McElwaine et al. 2000; Nishimura et al. 2005). Substituting the obtained snow depth and the air temperature into SSCM, the snow stability index (SI), which is the ratio of the shear stress to the shear strength of snow, was calculated. As shown in Fig. 4b, the SI values at both locations decreased to 2.0, which is much smaller than the value estimated at KA. Hirashima et al. (2006, 2008) set 2.0 as an appropriate SI threshold for evaluating avalanche susceptibility in Japan, indicating that the modeled avalanche danger level was high at both locations. Fortunately, there were no reported snow avalanche incidents during this period. However, it is clear that applying the observed snow depth at a given location in the study area is more appropriate for snow avalanche warning than the observed snow depth at KA.

4. Discussion and conclusions

We introduced a new set of procedures to evaluate snowdrift distribution over complex topography and improved the accuracy of snow avalanche warning systems. We selected the Niseko region as the target area due to dense coverage of weather stations across the region. We first obtained horizontal wind distribution maps at a 50-m grid spacing for the 16 wind directions. We then employed these wind maps to calculate the amount of snow erosion and deposition in each grid cell. Our February 2020 case study demonstrated that the model output agreed fairly well with the recorded wind speeds and snowdrift distribution observations across the area. Therefore, we can reasonably conclude that it is appropriate to incorporate our presented snowdrift analysis procedure into a snow avalanche warning system that employs the SSCM. In fact, when we applied the system to the avalanche release during the strong surface wind of nearly 20 m s^{-1} in Wakkanai, Hokkaido, it successfully indicates the avalanche danger level accurately, as is introduced in the Supplemental materials. However, there is still room for improvements as shown below.

We set KA as the reference point in the case study because a variety of meteorological data are available. However, as the reference point in the model we had to set the easternmost grid point at the same latitude as KA, since KA is outside of the model domain. Although the wind speeds and directions at both points were almost the same for all the wind directions, the model domain needed to be expanded to include KA. We note that the avalanche warning system should be combined with the hourly meteorological forecasts that are provided by JMA and the Japan Weather Association on a 1-km grid.

We divided the observed wind speeds at KA into three categories, less than 5, 5 to 10, and above 10 m s^{-1}, and obtained their associated snowdrift distribution with applying the result of 5 m s^{-1}, 10 m s^{-1} and 15 m s^{-1}, respectively. Thus, the degree of snow erosion and deposition might be overestimated. Although this approach was introduced to

reduce the computational requirements, the pitch of the wind speeds in the calculation should also be considered to further improve the accuracy of the model results. Further, the finer grid spacing might be taken into consideration. Although we used 50 m grid size to reduce the computational load, the higher-resolution simulations may be suitable to express the smaller-scale deposition pattern such as snow dunes and cornices (Mott and Lehning 2011).

The snowdrift distributions obtained in this study were qualitatively compared with visual observations. However, more precise observations in the target area, such as those obtained via airborne laser Doppler profiling, are desirable for a more quantitative comparison and a more accurate snowdrift evaluation. Furthermore, our simulation only employed a single snowdrift density of 100 kg m^{-3}, which is probably not always true; more realistic snowdrift densities should be considered. Precise data acquisition is also needed to better constrain future model simulations.

Snowdrifts generally develop over time during the winter season, and the topography of the snow surface changes accordingly. These drifts may then evolve substantially based on the wind speed and direction effects over the terrain. Such interactions between the wind field and snowdrift formation need to be considered to simulate snowdrift formation and evolution more precisely.

Acknowledgments We are grateful to Niseko Town and NIED for providing the wind data. We thank Dr. Yoichi Ito (NIED) for providing snowdrift information across the Mt. Annupuri region. This work was partly supported by JSPS KAKENHI Grant Number JP15H02992.

Edited by: M. Niwano

Supplements

Figs. S1 to S4: Application of SSCM and the snow drift simulation procedure in Wakkanai, Hokkaido.

References

Bagnold, R. A., 1941: The Physics of Blown Sand and Desert Dunes, Methuen, New York, 265 pp.

Brun, E., E. Martin, V. Simon, C. Gendre, and C. Coleou, 1989: An energy and mass model of snow cover suitable for operational avalanche forecasting. *J. Glaciology*, **35**, 333−342.

Hirashima, H., K. Nishimura, S. Yamaguchi, A. Sato, and M. Lehning, 2006: Evaluation of snow stability index in a snow cover model for avalanche accidents. *Cold Reg. Technol. Conf.*, **22**, 26−30 (in Japanese).

Hirashima, H., K. Nishimura, S. Yamaguchi, A. Sato, and M. Lehning, 2008: Avalanche forecasting in a heavy snowfall area using the snowpack model. *Cold Reg. Sci. Technol.*, **51**, 191−203.

Iversen, J. D., R. Greeley, B. R. White, and J. B Pollack, 1980: Eolian erosion of the Martian surface. Part I; Erosion rate similitude. *Icarus*, **26**, 321−331.

Kikuchi, T., 1981: Studies on aerodynamic surface roughness associated with drifting snow. *Mem. Fac. Sci. Kochi Univ.*, **2**, Ser. B, 13−37.

Komatsu, A., and K. Nishimura, 2020: A simple snow cover model for avalanche warning. *SOLA*, **16**, 246−251.

Lafore, J., J. Stein, N. Asencio, P. Bougeault, V. Ducrocq, J. Duron, and J. V.-G. de Arellano, 1998: The Meso-NH atmospheric simulation system. Part I: Adiabatic formulation and control simulations. *Annales Geophysicae*, **16**, 90−109.

Launder, B. E., and D. B. Spalding, 1974: The numerical computation of turbulent flow. *Comp. Meth. Appl. Mech. Eng.*, **3**, 269−289.

Lehning, M., H. Löwe, M. Ryser, and N. Raderschall, 2008: Inhomogeneous precipitation distribution and snow transport in steep terrain. *Water Resour. Res.*, **44**, W07404, doi:10.1029/2007WR006545.

McElwaine, J., A. Hachikubo, M. Nemoto, Y. Kaihara, T. Yamada, and K. Nishimura, 2000: Observations and simulations of the formation of the faceted snow crystals in the week-layer of the 1998 Niseko haru no Taki avalanche. *Cold Reg. Sci. Technol.*, **31**, 235−247.

Mott, R., and M. Lehning, 2011: Meteorological modeling of very high-resolution wind fields and snow deposition for mountains. *J. Hydrometeor.*, **11**, 934−949.

Murakami, S., K. Shunsuke, and Y. Ishida, 1989: Numerical simulation of room air flow with generalized curvilinear coordinates. *J. Archit. Plan. Environ. Eng.*, **400**, 39−49 (in Japanese with English abstract).

Nishimura, K., E. Baba, H. Hirashima, and M. Lehning, 2005: Application of the snow cover model SNOWPACK to snow avalanche warning in Niseko, Japan. *Cold Reg. Sci. Tech.*, **43**, 62−70.

Orlanski, U., 1976: A simple boundary condition for bounded hyperbolic flows. *J. Comput. Phys.*, **21**, 251−269.

Patankar, S. V., 1981: Numerical Heat Transfer and Fluid flow. Hemisphere, Washington, D. C., 193 pp.

Sato, T., and F. Yasuda, 2014: A numerical simulation of snowdrift around blower snow fence. *Proc. Cold Reg. Technol. Conf.*, **30**, 47−52 (in Japanese).

Uematsu, T., K. Nakata, K. Takeuchi, Y. Arisawa, and Y. Kaneda, 1991: Three-dimensional simulation of snowdrift. *Cold Reg. Sci. Tech.*, **20**, 65−73.

Vionnet, V., E. Martin, V. Masson, C. Lac, F. Naaim Bouvet, and G. Guyomarc'h, 2017: High-resolution Large Eddy simulation of snow accumulation in alpine terrain. *J. Geophys. Res. Atmos.*, **122**, 11005−11021.

Xue, M., K. K. Droegemeier, V. Wong, A. Shapiro, and K. Brewster, 1995: ARPS version 4.0 user's guide. *Center for Analysis and Prediction Of Storms, University of Oklahoma*, Norman, Okla, 380 pp.